3D modelling of stellar auroral radio emission

P. Leto,[1]⋆ C. Trigilio,[1]⋆ C. S. Buemi,[1] G. Umana,[1] A. Ingallinera[1] and L. Cerrigone[2]

[1]*INAF – Osservatorio Astrofisico di Catania, Via S. Sofia 78, 95125 Catania, Italy*
[2]*ASTRON, Netherlands Institute for Radioastronomy, PO Box 2, 7990 AA Dwingeloo, the Netherlands*

ABSTRACT

The electron cyclotron maser is the coherent emission process that gives rise to the radio lighthouse effect observed in the hot magnetic chemically peculiar star CU Virginis. It has also been proposed to explain the highly circularly polarized radio pulses observed in some ultracool dwarfs with spectral type earlier than M7. Coherent events of this kind resemble auroral radio emission from the magnetized planets of the Solar system. In this article, we present a three-dimensional model able to simulate the timing and profile of the pulses emitted by those stars characterized by a dipolar magnetic field by following the hypothesis of the laminar source model, used to explain the beaming of terrestrial auroral kilometric radiation. This model proves to be a powerful tool with which to understand the auroral radio emission phenomenon, allowing us to derive some general conclusions about the effects of the model's free parameters on the features of coherent pulses and to learn more about the detectability of such pulsed radio emission.

Key words: masers – polarization – stars: chemically peculiar – stars: magnetic field.

1 INTRODUCTION

The electron cyclotron maser (ECM) is a coherent emission mechanism excited by the inverse velocity distribution that an electron population propagating along the converging field lines of a density-depleted magnetospheric cavity can develop. This mechanism (Wu & Lee 1979; Melrose & Dulk 1982) amplifies the extraordinary magneto-ionic mode, producing almost 100 per cent circularly polarized radiation at a frequency close to the local gyrofrequency ($\nu_B \propto B$). Maser amplification can occur within a magnetospheric region covering a wide range of magnetic field strength, providing observable ECM emission over a wide frequency range. The ECM is the mechanism responsible for broad-band auroral radio emission from the magnetized planets of the Solar system, such as terrestrial auroral kilometric radiation (AKR), Jupiter decametre (DAM), hectometre (HOM) and kilometre (KOM) emission, Saturn kilometric radiation (SKR), Uranus kilometric radiation (UKR) and Neptune kilometric radiation (NKR) (Zarka 1998). The angular beaming of the Earth's AKR observed with the spacecraft array *Cluster* (Mutel, Christopher & Pickett 2008) confirms that the Earth's ECM emission pattern is strongly anisotropic. Such terrestrial coherent emission is confined within a narrow beam directed tangentially along the walls of the auroral cavity where the amplification mechanism occurs. In the framework of the laminar source model (Louarn & Le Queau 1996a,b), such anisotropy of the ECM radiation pattern is a direct consequence of the small thickness of the cavity. In fact,

the radiation path in the direction perpendicular to the cavity walls is too short to give significant amplification. The AKR will then be refracted upwards by the highest-density regions when it leaves the cavity (Mutel et al. 2008; Menietti et al. 2011).

Auroral radio emission has also been observed in stars. In particular, such a phenomenon has been well studied in the case of CU Vir, a magnetic chemically peculiar (MCP) star. MCPs are early-type main-sequence stars, characterized by strong magnetic fields with a mainly dipolar topology, the axis of which is tilted with respect to the rotational axis (oblique rotator). Non-thermal incoherent radio emission from MCPs has been detected in almost 25 per cent of cases (Drake et al. 1987; Linsky, Drake & Bastian 1992; Leone, Trigilio & Umana 1994). In accordance with the oblique rotator model (ORM), the radio emission is also periodically variable as a consequence of stellar rotation (Leone 1991; Leone & Umana 1993), suggesting that this radio emission arises from a stable rigidly corotating magnetosphere (RRM). This variability has been reproduced successfully by a three-dimensional (3D) model able to compute the gyrosynchrotron emission from an RRM in the framework of the ORM (Trigilio et al. 2004; Leto et al. 2006).

The radio emission from the MCPs is ascribed to a radiatively driven stellar wind. Far from the star, specifically on the magnetic equator at about the Alfvén radius, this wind opens the magnetic field lines, forming current sheets. The reconnection of the low-strength magnetic field lines accelerates electrons up to relativistic energy. The thin transitional magnetospheric layer between the inner and dense magnetospheric regions (the region where the confined plasma accumulates) and the escaping wind is named the 'middle

⋆ E-mail: Paolo.Leto@oact.inaf.it (PL); corrado.trigilio@oact.inaf.it (CT)

magnetosphere'. The energetic electrons that recirculate through this layer back to the stellar surface radiate radio waves by an incoherent gyrosynchrotron emission mechanism. The middle magnetosphere is also the region where the conditions for triggering the ECM mechanism could be realized. In fact, the relativistic electron population, accelerated far from the star, moves along converging dipolar field lines towards the high-strength magnetic field regions close to the stellar surface. Moreover, due to magnetic mirroring, only energetic electrons with very low pitch angle (electron path almost parallel to the magnetic field lines) can impact the stellar surface and will be lost. The reflected non-thermal electron population could then develop the inversion of the velocity distribution needed to trigger the ECM mechanism. Other kinds of unstable energy distribution can be developed by the precipitating non-thermal electron beams, such as the horseshoe distribution, able to produce ECM emission efficiently (Ergun et al. 2000).

In spite of the favourable physical conditions that characterize the magnetospheres of radio MCP stars, only CU Vir and HD 133880 are so far characterized by broad-band, highly polarized and time-stable pulses (Trigilio et al. 2000, 2008, 2011; Ravi et al. 2010; Lo et al. 2012; Chandra et al. 2015), ascribed to auroral radio emission detected when the magnetic dipole axis is almost perpendicular to the line of sight. The frequency of the ECM emission observed from CU Vir ranges from about 600 MHz (Stevens & George 2010) to 5 GHz (tentative detection reported by Leto et al. 2006), whereas for HD 133880 a detection of ECM emission at 600 MHz and 1.4 GHz has been reported (Chandra et al. 2015).

CU Vir is the first star for which stellar auroral radio emission was detected (Trigilio et al. 2000). For this star, the coherent emission process was mainly observed and studied extensively at frequencies of 1.4 and 2.5 GHz (Trigilio et al. 2000, 2008, 2011; Ravi et al. 2010; Lo et al. 2012). It shows two pulses per spin period, almost 100 per cent right-hand circularly polarized, with a phase separation of ≈0.4, characterized by a frequency drift of the pulse arrival time. Two pulses per period have been detected at 1.4 GHz in every observing epoch, unlike the auroral radio light curve at 2.5 GHz, which does not always show two pulses per period. Moreover, left-handed circularly polarized pulses were never detected from CU Vir. This lack of left-hand polarization has been explained as due to the non-perfectly dipolar topology of its magnetic field (Kochukhov et al. 2014). The existence of multipolar magnetic field components makes the behaviour of the two opposite hemispheres asymmetric. In addition, the existence of a multipolar field topology has been indicated as the cause of the absence of auroral radio emission in σ Ori E (Leto et al. 2012), another well-studied radio MCP star characterized by a non-simple dipole field (Oksala et al. 2012).

Similarly to the Earth's AKR, the coherent pulses observed from CU Vir were explained as ECM emission originating in an auroral cavity, tangentially beamed to the walls and then refracted upward (Trigilio et al. 2011). This anisotropic beaming is able to reproduce successfully the timing and pulse width of the auroral radio emission observed in CU Vir (Lo et al. 2012).

At the bottom of the main sequence, coherent pulses, still explained as auroral radio emission due to the ECM, were also observed in some ultracool dwarfs (UCDs) with spectral type earlier than M7 (Berger 2002; Burgasser & Putman 2005; Antonova et al. 2008; Hallinan et al. 2008; Route & Wolszczan 2012, 2013; Williams et al. 2015), showing in some cases features similar to those observed in CU Vir. For example, the M8 dwarf DENIS-P J1048.0 − 3956 shows time-shifted pulses at 5 and 8.4 GHz, both fully right-hand circularly polarized (Burgasser & Putman 2005), and the T6.5 brown dwarf 2MASSI J1047539 + 212423 is
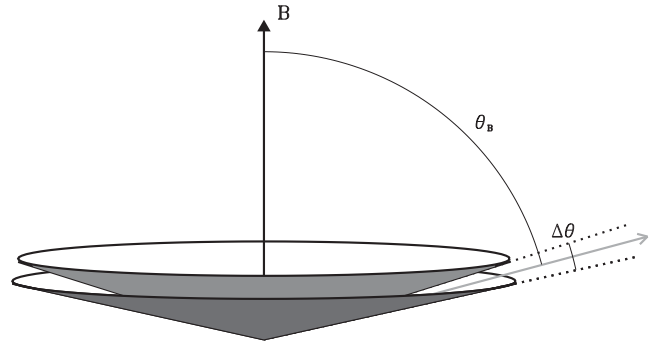
Figure 1. Beaming pattern of the loss-cone-driven ECM elementary emission process. The amplified radiation, displayed by the light grey vector, is emitted within a hollow cone centred on the local magnetic field vector (B) of half-aperture $\theta_{\rm B}$ and thickness $\Delta\theta$.

characterized by left-hand circularly polarized periodic pulses detected at 6 GHz (Williams et al. 2015). For the ultracool dwarfs has also been highlighted as coherent events, such as this, could have a role as ionizing factors of their atmospheres (Vorgul & Helling 2016).

In the framework of the laminar source model, in this article we develop a 3D model of auroral radio emission from stars with a dipole-like magnetic field. This model is used to study how auroral radio emission features depend on stellar geometry and on the parameters that define the ECM beam pattern. This study was able to give a deeper insight into the relationship between auroral radio emission detectability and model parameters.

2 THE AURORAL RADIO EMISSION MODEL

For the ECM emission driven by loss-cone instability, the radiation amplified by this kind of coherent emission process is beamed in a very thin hollow cone centred on the local magnetic field line (Wu & Lee 1979; Melrose & Dulk 1982). The radiation cone has half-aperture $\theta_{\rm B} \approx \arccos(v/c)$, where v is the speed of the unstable electron population (Hess, Cecconi & Zarka 2008). In the case of 2-keV energy electrons, the hollow cone half-aperture is ≈85°. To explain the geometry of the elementary emitting process clearly, a thin conical sheet of thickness $\Delta\theta$ has been shown in Fig. 1. The frequency ν of the amplified radiation has to satisfy the cyclotron resonance condition for transverse emission $\nu = s\nu_{\rm B}/\gamma$, where s is the harmonic number of the local gyrofrequency ($\nu_{\rm B} = 2.8 \times 10^{-3}B/{\rm G}$ GHz) and for mildly relativistic electrons the Lorentz factor $\gamma \approx 1$. The fundamental harmonic ($s = 1$) has the fastest growth rate, but it is likely suppressed by gyromagnetic absorption as it crosses the more external layer in which the second harmonic of the local gyrofrequency is equal to the amplified frequency. The layers at $s > 2$ have lower optical depth for gyromagnetic absorption; it is thus reasonable to assume that, when detected, ECM emission occurs at $\nu = 2\nu_{\rm B}$ (Melrose & Dulk 1982).

In the case of ECM amplification occurring in thin magnetospheric cavities (laminar source model), the resulting overall radiation diagram can be strongly anisotropic (Louarn & Le Queau 1996a,b) and the axial symmetry of the single-electron emission beam will be lost. In fact, elementary ECM sources with similarly oriented emission beam pattern and located along the line of sight all contribute together to the maser amplification. If the cavity has a laminar structure, the rays tangent to the walls maximize the path within the region where the ECM originates. Theoretical simulations also confirm that auroral radio emission is mainly amplified
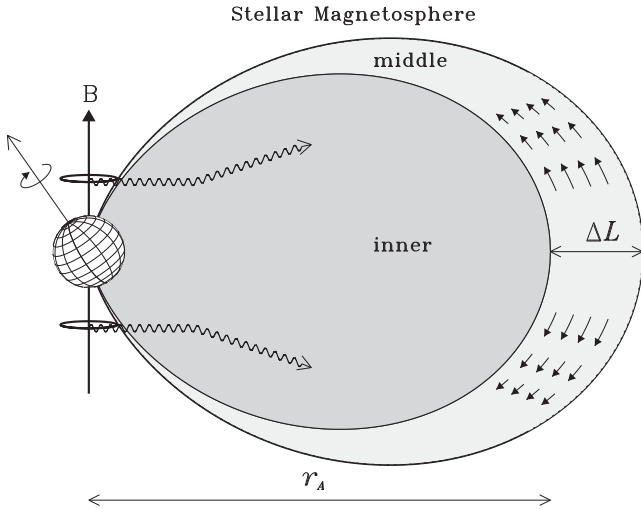
Figure 2. Section of a dipole-like magnetosphere where auroral radio emission can take place. The magnetospheric size is defined by the Alfvén radius r_A, whereas the thickness (ΔL) of the auroral cavity is defined by the length of the current sheet where the free electrons are accelerated up to relativistic energy. Non-thermal electrons (represented by small solid arrows) move towards the stellar surface within a transitional layer named the middle magnetosphere. Above the magnetic poles, close to the stellar surface, the two auroral rings where the ECM arises are located. The amplified radiation (the two waves displayed in the northern and southern hemispheres) is emitted tangentially to the ring and then refracted upward by the dense thermal plasma trapped inside the inner magnetosphere.

tangentially to the cavity boundary, rather than along the perpendicular direction (Speir et al. 2014). The resulting ECM emission is beamed in a strongly directive radiation diagram and will then be detectable only when our line of sight crosses the radiation beam pattern, like the pulses of a radio lighthouse.

We will analyse the auroral radio emission from a dipole-like magnetospheric cavity in the framework of the laminar source model described above. The magnetosphere is assumed to be a simple dipole tilted with respect to the rotation axis. Within a fixed value of equatorial radius (the Alfvén radius, r_A), thermal plasma accumulates (inner magnetosphere), while beyond the Alfvén radius the plasma breaks the magnetic field lines, giving rise to a density-depleted magnetospheric cavity (middle magnetosphere) where non-thermal electrons can propagate freely, accelerated by magnetic reconnection (see Fig. 2). This population of non-thermal electrons can develop an unstable energy distribution, able to pump the electron cyclotron maser. The overall behaviour of the ECM emission process that can take place in this kind of magnetospheric cavity (schematically pictured in Fig. 2) is described as follows: the ECM radiation arising from a generic point of the auroral ring propagates in the plane of the ring; following the laminar source model, coherent emission is beamed along the plane parallel to the magnetic axis and tangent to the ring; the auroral radio emission is then refracted upward by the dense thermal plasma trapped within the inner magnetosphere. To study the features of the ECM pulses arising from such an auroral cavity, we use the same approach followed by Trigilio et al. (2004) and Leto et al. (2006). In these works, we simulated the incoherent gyrosynchrotron brightness distribution and the total flux density by sampling the space surrounding the star. Given physical parameters such as the local magnetic field strength and orientation, the thermal and non-thermal electron number density, etc., we calculated at every grid point the local emission and

absorption coefficients for the gyrosynchrotron mechanism, which are needed to integrate the radiative transfer equation along the line of sight. In the present work, we do not integrate the radiative transfer equation for the ECM. We only search for those spatial points that satisfy the physical conditions required for electron cyclotron maser generation at a given frequency and have a radiation beam pattern oriented along the line of sight. The modelling approach developed in this article is limited only to the study of the timing and profile of ECM pulses, which depends on those parameters that define the geometric conditions able to make such a phenomenon detectable.

As a first step, we set the stellar geometry (i is the inclination of the rotation axis, β the tilt of the dipole magnetic axis and Φ the rotation phase) and the polar field strength. The rotation axis, which is misaligned with respect to the magnetic polar axis, is displayed in Fig. 2. In the stellar reference frame, the space surrounding the star is sampled using a 3D Cartesian grid and at each grid point the dipolar magnetic field vector components are calculated. The vectorial field is then rotated in the observer's reference frame (see appendix A of Trigilio et al. 2004).

As a second step, we localize the magnetospheric cavity where the unstable electron population propagates. The inner and outer boundary dipolar field lines are defined by the equation $r = L\cos^2\lambda$, where r is the distance to the centre of the star and λ the magnetic latitude. This space region intercepts the magnetic equatorial plane at distances L and $L + \Delta L$ from the centre of the star, respectively, for the inner and outer boundary. These magnetic field lines are shown in Fig. 2. Within the magnetic shell thus defined, we can find the set of grid points that has the same value of local magnetic field strength. Given the frequency ν of the observable coherent emission, we are hence able to localize those grid points that have $2\nu_B = \nu$, within a fixed bandwidth $\Delta\nu$. These points are distributed in polar rings above the magnetic poles. The northern and southern auroral rings that emit the ECM at an arbitrary frequency are displayed in Fig. 2. Given the boundary magnetic field lines, the radius and height above the stellar surface of these rings follow the radial dependence of the magnetic field strength B, which defines the gyrofrequency.

The third step consists of the definition of the emission-beam pattern of each grid point belonging to the auroral rings. For clarity, the side and top view of the ECM emission diagram arising from the northern ring are displayed in the two panels of Fig. 3. Each point of the auroral ring, which is the source of ECM emission at frequency ν, has an emission diagram defined by the following angles: deflection angle θ; opening angle $\Delta\theta$; beaming angle δ. The angle θ is defined as the angle between the ray-path vector $\boldsymbol{k}$ and the plane containing the ring (which is perpendicular to the magnetic dipole axis). $\Delta\theta$, set equal to $5°$, is the hollow-cone thickness (see Fig. 1), which in the case of loss-cone driven instability is a function of the emitting electron speed, $\Delta\theta \approx v/c$ (Melrose & Dulk 1982) and, in accord with Trigilio et al. (2000), this speed has been fixed equal to $0.09c$ (electron energy ≈ 2 keV), corresponding to an emitting conical sheet just $5°$ thick. The angle δ accounts for the width of the radiation diagram centred on the plane tangent to the auroral circle and parallel to the magnetic axis. This angle has the aim of parametrizing the number of elementary ECM sources located in the auroral rings, with emission beams closely aligned with the line of sight (the beam width is highlighted by the grey planes in Fig. 3). When the line of sight passing through a given grid point located on the auroral circle is tilted with respect to the local magnetic field vector of angle $90° - \theta$ (for ECM sources in the northern magnetic hemisphere) or $90° + \theta$ (for sources in the southern hemisphere) within $\Delta\theta/2$ and forms an angle lower then $|\delta/2|$ with the plane

(a)

(b)
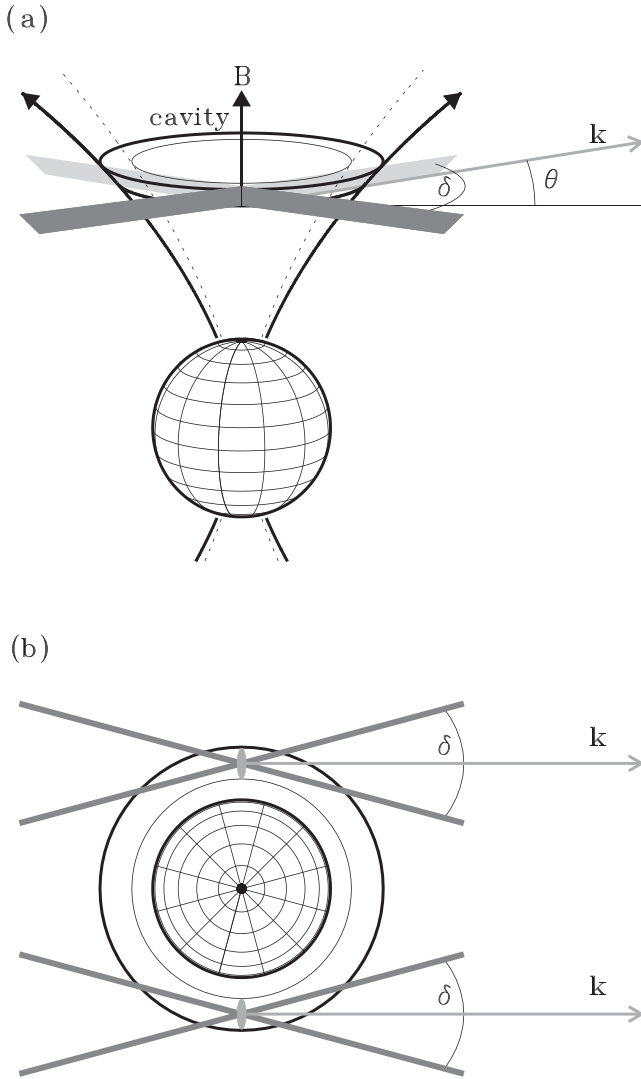
Figure 3. Schematic view of the model of the auroral radio emission developed in the framework of the laminar source model. (a) Side and (b) top views are shown. The density-depleted magnetic cavity and the boundary field lines are shown. A representative auroral ring is also displayed above the north pole, where the ECM emission process originates. The grey planes passing trough the boundary of the cavity describe the ECM beam pattern, the size of which is given by the angle δ. The ECM ray vector (k) is misaligned by an angle θ with respect to the direction perpendicular to the local magnetic field vector (B).

tangent to the auroral ring, the corresponding grid point will be assumed to be an observable source of ECM emission.

To separate the contributions of ECM emission arising from the two opposite magnetic hemispheres, we assign right-hand circular polarization (RCP) to the emission from sources in the northern hemisphere and left-hand circular polarization (LCP) to the emission from southern ones. If we repeat the operations explained above as a function of the stellar rotation phase and store the number of grid points that are ECM sources, along with their corresponding polarization sense, then we are able to simulate the features of the ECM light curves for the I and V Stokes parameters (respectively defined as RCP + LCP and RCP − LCP).

As a further output, once we set the stellar parameters that describe the geometry and strength of the dipolar field, the 3D model provides us with the effective magnetic field curve. In fact,

simulations of ECM emission require the calculation of the vectorial field generated by the magnetic dipole. For a given rotational phase, we are able to calculate the longitudinal component of each magnetic field vector located on the stellar surface. The sum of such longitudinal components, weighted by the limb-darkening law, gives us the theoretical effective magnetic field strength (B_e) as a function of the stellar rotation. In detail, a calculation has been performed as follows:

$$B_e = \frac{\sum_x \sum_y \sum_z B_x(x, y, z) I(x, y, z)}{\sum_x \sum_y \sum_z I(x, y, z)},$$

where B_x is the longitudinal component of the magnetic field vector located at coordinate (x, y, z) on the side of the stellar surface facing the observer and I is the corresponding limb-darkening parameter. The observing reference frame ($Oxyz$) is centred on the stellar centre, the x-axis is aligned with the line of sight and oriented towards the observer and the y and z-axes delineate the plane of the sky. Each point of the grid is associated with the vector $\mathbf{r} \equiv (r_x, r_y, r_z)$ and the points located on the stellar surface are those that verify, within the sampling step, the condition $r_x^2 + r_y^2 + r_z^2 = 1$ (assuming a unitary stellar radius). For the calculation, we have adopted a simple linear limb-darkening law:

$$I(x, y, z) = 1 - k + k r_x(x, y, z) \qquad (0 \le r_x \le 1)$$

with $k = 0.45$ (Stift 1973). Therefore, with the capability of simultaneously simulating the ECM light curve and the magnetic curve, we can correlate ECM occurrence with the B_e curve.

3 MODEL PREDICTIONS

3.1 Dependence on the auroral ring geometry

First of all, we analyse whether the spatial location and size of the auroral regions that are sources of ECM emission affect the simulated light curves. To do this, we set the magnetic field and vary the frequency; this is equivalent to simulating ECM emission from auroral rings of different sizes and locations above the stellar surface.

We simulated a set of frequencies ranging from 600 MHz to 5 GHz. For this specific analysis, the stellar geometry and ECM radiation diagram are fixed. We assumed a dipole with a polar field strength of 3000 G, misaligned with respect to the rotation axis of an angle $\beta = 74°$; the rotation axis inclination (i) has been fixed to 43°. The parameters above are equal to the stellar parameters adopted for CU Vir (the prototype of stars showing auroral radio emission) by Trigilio et al. (2000). The thickness of the magnetic shell that delimits the auroral cavity has been defined by setting the L-shell parameter of the two boundary dipolar magnetic field lines equal to 15 and $18R_*$ ($\Delta L = 20$ per cent of L), respectively, in accordance with the size of the magnetospheric region where the incoherent radio emission of CU Vir originates (Leto et al. 2006). The two boundary magnetic field lines have maximum separation at the magnetic equator, whereas at the stellar surface these two field lines are very close. For the ECM emission beam pattern, we assume the simple condition of amplified radiation propagating perpendicularly to the local magnetic field vector (no refraction, $\theta = 0°$) with a narrow radiation diagram (opening angle fixed to $\delta = 10°$).

The spatial distribution of the ECM emission, calculated when the magnetic dipole axis lies exactly in the sky plane (null value of effective magnetic field), has been displayed in the top panels of Fig. 4. The simulated maps were obtained by collecting the ECM
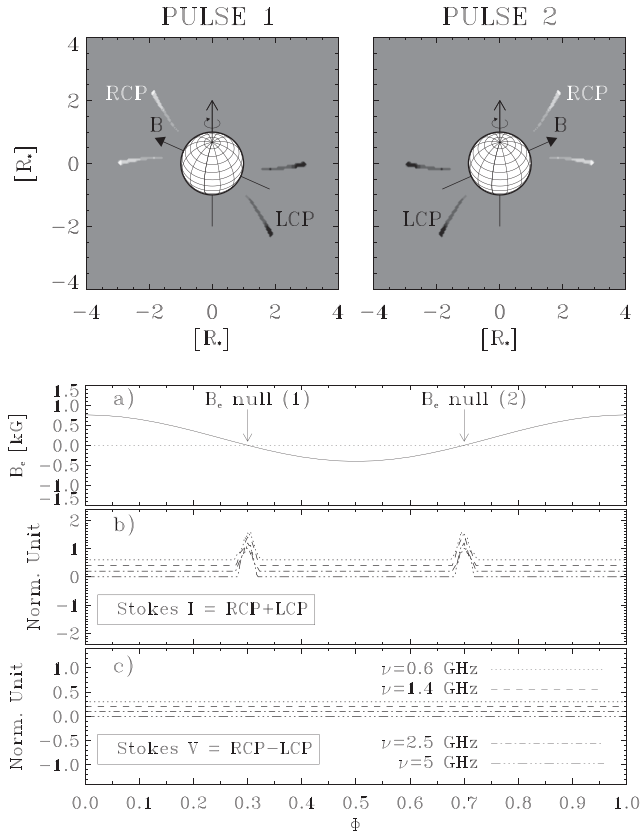
Figure 4. Top panels: wide-band synthetic brightness spatial distribution of the ECM emission arising from the two opposite hemispheres of a dipole-like oblique rotator. The maps have been created for the two stellar orientations where the longitudinal magnetic field is null. The simulated frequencies range between 5 GHz (close stellar regions) and 600 MHz (farther away regions). The emission that originates from the northern hemisphere is shown by the white area, while the dark area is associated with ECM emission from the southern hemisphere. Bottom panels: (a) simulated magnetic curve; (b) and (c) ECM light curves simulated at $\nu = 0.6$, 1.4, 2.5 and 5 GHz, respectively, for Stokes I and V. An arbitrary offset has been added to each individual light curve to distinguish them.

contributions from all grid points (simulation step equal to $0.05R_*$) that have the second harmonic of the local gyrofrequency in the range 600 MHz–5 GHz.

In accordance with the radial dependence of the magnetic field strength, decreasing outward as r^{-3} for a dipole, the highest frequencies originate in small auroral rings located near the star; the low frequencies are instead generated in large auroral rings at high distances above the stellar surface. The simulated frequencies originate from auroral rings located between ≈ 0.5 and $2R_*$ from the stellar surface. The ECM emission at 5 GHz is generated within the thin auroral cavity located close to the star, unlike the ECM radiation at 600 MHz, which arises from auroral regions far from the star and is consequently generated within a larger and thicker auroral cavity.

The model predicts similar ECM light curves at different simulated frequencies (small differences are due to the sampling effect) characterized by two peaks per stellar rotation, visible when $B_e = 0$. The theoretical magnetic curve and the corresponding ECM light curves for Stokes I and V are displayed in the three bottom panels of Fig. 4, simulated setting $\nu = 0.6$, 1.4, 2.5 and 5 GHz. As a consequence of the chosen stellar geometry (assumed equal to

the prototype CU Vir), the minimum phase difference between the two simulated ECM peaks is about 0.4, which is in accordance with the phase difference between the two coherent events observed for CU Vir.

By inspecting the simulated light curves for the two Stokes parameters, we can see that there is no Stokes V (RCP − LCP) contribution, whereas the Stokes I (RCP + LCP) is clearly observable. This is because the ECM contributions from the two opposite magnetic hemispheres are exactly the same, as is evident by the perfect symmetry of the ECM brightness spatial distribution (top panel of Fig. 4). Since the ECM radiation arising from the two hemispheres has opposite polarization senses in the north and in the south, the Stokes V parameter will consequently be null.

3.2 Dependence on the beam pattern

To assess the effect of the free parameters that control the beam pattern of the ECM radiation on the auroral radio emission features, we simulated the light curves by varying the opening angle δ and the upward deflection angle θ, keeping the stellar geometry previously adopted. In this case, we performed simulations of ECM emission at 2.5 and 1.4 GHz. To mitigate the possible bandwidth effect, which could affect the comparison between simulations and most available observations, these simulations have been performed within a narrow frequency range, 100 MHz wide, which is close to the old Very Large Array (VLA) and Australia Telescope Compact Array (ATCA) bandwidth set-up. For the assumed polar field strength ($B_e = 3000$ G), the two auroral rings are located respectively at ≈ 0.9 and $1.3R_*$ above the magnetic poles. The results of the simulations for the Stokes parameters I and V are displayed in Fig. 5, where the right circularly polarized emission (positive Stokes V) is displayed in white and the left circular polarization (negative Stokes V) in black. In each panel of Fig. 5, for a given angle δ, the dynamical simulated light curves are displayed as a function of the angle θ, shown on the y-axis.

First of all, we notice that the light-curve features of the auroral radio emission at the two simulated radio frequencies – 1.4 and 2.5 GHz – have a closely similar dependence on the two parameters δ and θ. This is equivalent to saying that the spatial location and size of the auroral rings have little or no effect on the main features of the auroral radio emission, once the auroral cavity is defined. The timing and pulse profile are instead significantly affected by the choice of δ and θ. In particular, the dynamic light curves of the Stokes I parameter show that the pulse width is directly related to the angle δ, with narrow peaks associated with smaller δ values. We also note that the pulses disappear above a deflection-angle limit. This trend is observable for each value of the parameter δ, with the limiting value of the angle θ growing as δ increases. It is also evident that, before disappearing, each pulse splits in two, with the phase separation growing with θ. By analysing the Stokes V, it is clear that each component of the double-peak pulses has opposite polarization sense. In general, Stokes V has a hybrid polarization, as a consequence of the different contributions to the ECM emission of the two stellar hemispheres with opposite magnetic polarity. As a consequence of the physical processes that are responsible for the generation and propagation of ECM emission, the deflection angle θ could be a function of frequency. In fact, the basic processes that drive the ECM (like the loss-cone instability) originate amplified radiation propagating in direction that is frequency-dependent, or/and the refraction effects (which can be suffered by the amplified radiation travelling through cold thermal plasma layers) are also function of the frequency. By comparing multifrequency observations and

Stokes I

Stokes V
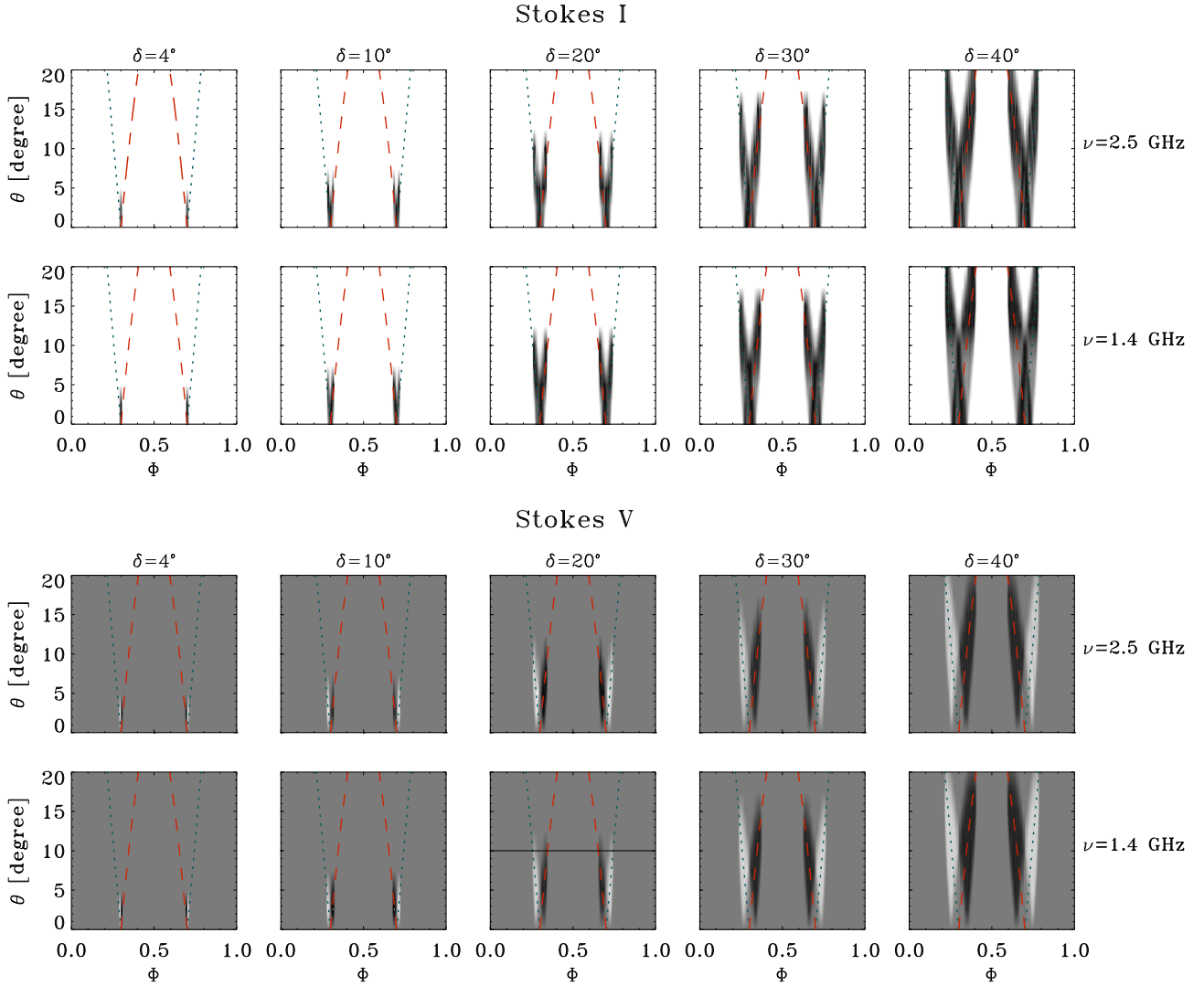
Figure 5. Dynamic ECM light-curve results of the 3D model simulations obtained by varying the parameters that control the radiation beam pattern. The simulated frequencies are 1.4 and 2.5 GHz. The model simulations have been performed as a function of the ray-path deflection θ (y-axis of each panel). The simulations have been performed for five values of the opening angle δ. The top panels display the Stokes I parameter, while the bottom panels display Stokes V; black corresponds to the left-hand circularly polarized component, while white indicates right-hand polarized. The pulse phase location predicted by the ORM has also been shown; the dotted line is related to the ECM pulses arising from the northern hemisphere, while the dashed line is referred to the southern. The black continuous line in the panel with the simulations performed at $\nu = 1.4$ GHz and $\delta = 20°$ is a representative light curve obtained assuming $\theta = 10°$.

simulations, we will be able to measure the deflection angle of each individual amplified frequency and thus we can try to disentangle the possible frequency-dependent mechanism that would affect the propagation direction of this kind of amplified emission.

The pulse timing is the result of the oblique rotator model assumption. In fact, the upward deflection angle θ is related to the angle formed by the line of sight with the magnetic dipole axis (θ_M) as follows:

$$\theta_M = \begin{cases} \pi/2 - \theta, & \text{northern hemisphere,} \\ \pi/2 + \theta, & \text{southern hemisphere.} \end{cases}$$

Once the ORM geometry (i and β) is defined, the phase location of the ECM pulse is expressed by the following equation (Trigilio et al. 2000):

$$\Phi_{ECM} = \arccos\left(\frac{\cos\theta_M - \cos\beta\cos i}{\sin\beta\sin i}\right)/2\pi. \quad (1)$$

The tracks of the ECM pulses calculated with the use of equation (1) have been placed on top of the simulated light curves in Fig. 5. The comparison between the model simulation and the ORM prediction indicates that the phase location of each ECM peak can be predicted by equation (1), whereas the ECM pulse profile is the result of a complicated combination of the angles that control the beam of the auroral radio emission.

To clarify the above model prediction better, the 1.4-GHz Stokes V synthetic light curve obtained with $\delta = 20°$ and $\theta = 10°$ has been analysed (it is identified in Fig. 5 by the black line). This selected light curve is shown in Fig. 6, along with the stellar magnetic curve. The stellar orientations associated with the various pulse components and identified on this simulated light curve have also been displayed. For clarity, each pulse component has been assigned a label related to the order of appearance and to the polarization sense. The ECM ray vectors have been tagged according to the labels of the corresponding simulated coherent pulse components.
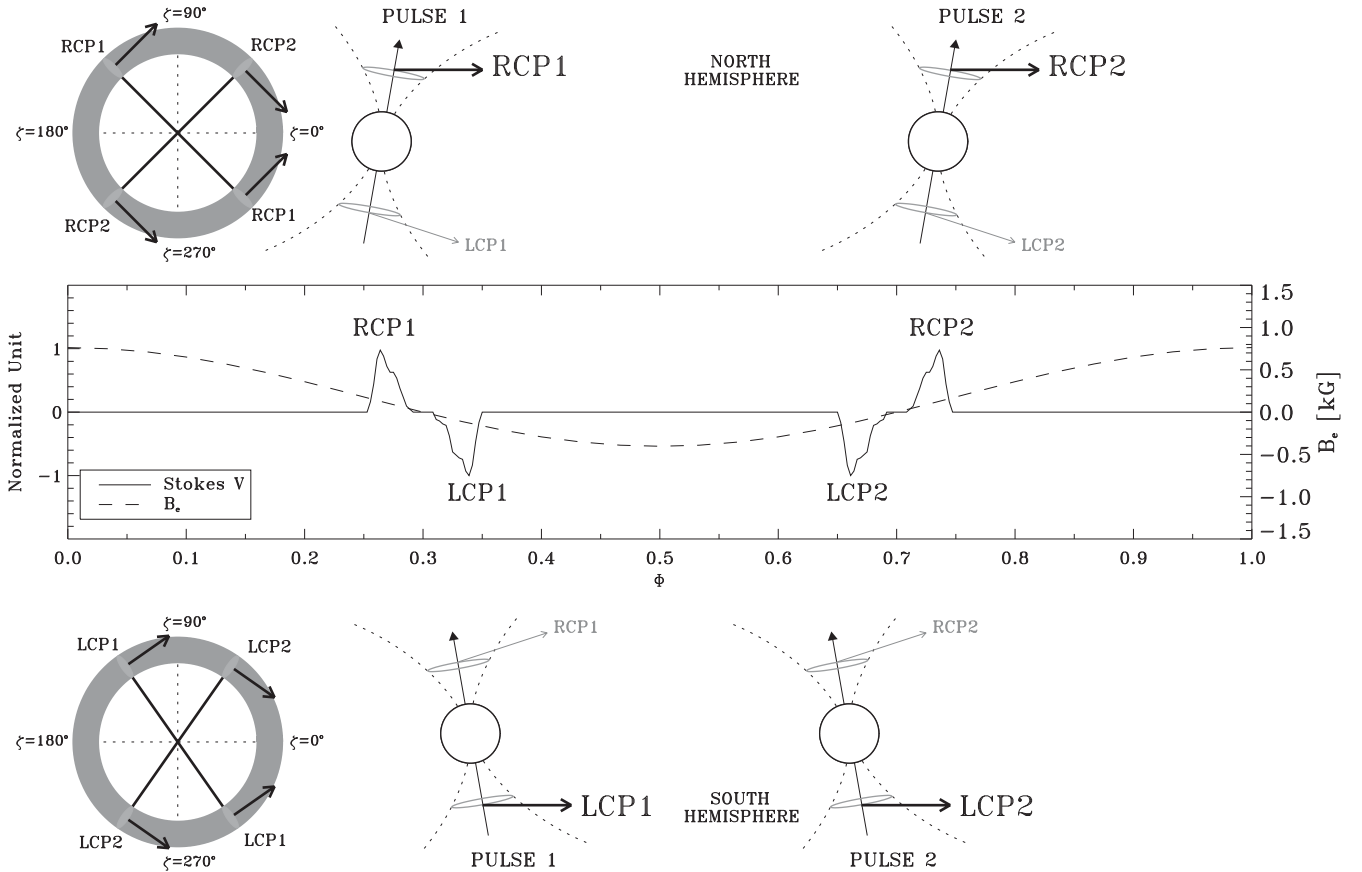
Figure 6. Synthetic auroral radio light curve (obtained assuming $\nu = 1.4$ GHz, $\delta = 20°$ and $\theta = 10°$: solid line), with the simulated effective magnetic field curve ($B_{\rm p} = 3000$ G, $i = 47°$, $\beta = 74°$: dashed line) superimposed. The pulses have been labelled as in Fig. 4, according to the arrival order and the circular polarization signs. The cartoons show the magnetosphere orientations corresponding to the beam of the auroral radio emission aligned with the line of sight. The two unit circles indicate the magnetic longitudes (ζ) of the magnetic field lines responsible for the auroral radio emission observable from the Earth.

The ECM emission beam pattern responsible for the first right-hand circularly polarized peak (RCP1) arising from the northern auroral ring is aligned with the line of sight at phases slightly preceding the first null of the magnetic curve, depending on θ (Fig. 6). As the star rotates, the northern pole will be seen moving away from the observer and, after the magnetic curve passes the first null, the ECM emission arising from the southern auroral ring will be visible (first left-hand circularly polarized pulse: LCP1). After that, the magnetic curve has reached its negative magnetic outermost point: the magnetic north pole will be seen approaching the observer and a second ECM beam generated from the southern auroral ring will be aligned with the line of sight. Consequently, the second LCP pulse will be detectable (LCP2). Likewise, the second RCP pulse will be associated with a second ECM beam arising from the northern auroral ring (RCP2).

The two ECM beams do not arise from the same points of the auroral circle. For clarity, in Fig. 6 we also included the auroral circles showing the magnetic longitudes ζ ($\zeta = 0°$ on the plane identified by the magnetic and rotation axis) of the magnetic field lines responsible for the detectable auroral radio emission. Such magnetic field lines intercept the northern and southern auroral rings in the two sectors, characterized by the ECM beam pattern crossing the observer's line of sight. In particular, for the specific case analysed here, the magnetic longitudes of the field lines that have the most favourable orientation for auroral radio emission to be detected are as follows, respectively: $\zeta \approx 135°$ and $\zeta \approx 315°$ (peak RCP1); $\zeta \approx 45°$ and $\zeta \approx 225°$ (peak RCP2);

$\zeta \approx 125°$ and $\zeta \approx 305°$ (peak LCP1); $\zeta \approx 55°$ and $\zeta \approx 235°$ (peak LCP2).

3.3 Dependence on the magnetic shell size

We performed model simulations of the auroral radio emission arising from magnetic shells with sizes different from the one previously analysed. The simulated ECM frequency and the radiation beam pattern were left unchanged ($\nu = 1.4$ GHz, $\delta = 20°$ and $\theta = 10°$). We analyse the cases of auroral cavities delimited by the inner-boundary magnetic field lines with L-shell parameter ranging from 5–100R_*. In addition, the magnetic shell thickness at the equatorial plane has been varied in the range of 10–50 per cent of the L parameter of the inner boundary magnetic field line.

The simulated dynamic ECM light curves (Stokes I and V) as a function of auroral cavity size have been displayed in Fig. 7. Each column of Fig. 7 shows the simulations performed assuming a different thickness of the magnetic cavity. Similarly to the previously adopted grey-scale for the Stokes V simulations, the white regions indicate ECM emission that has a right-hand circular polarization sense, whereas the black areas refer to radiation with left-hand circular polarization.

The result of these simulations highlights that the size of the auroral cavity significantly affects the pulse profile. The simulations of auroral radio emission for Stokes I arising from small magnetic shells are characterized by two large pulses per stellar rotation; see the top panels of Fig. 7. As the size of the magnetic shell
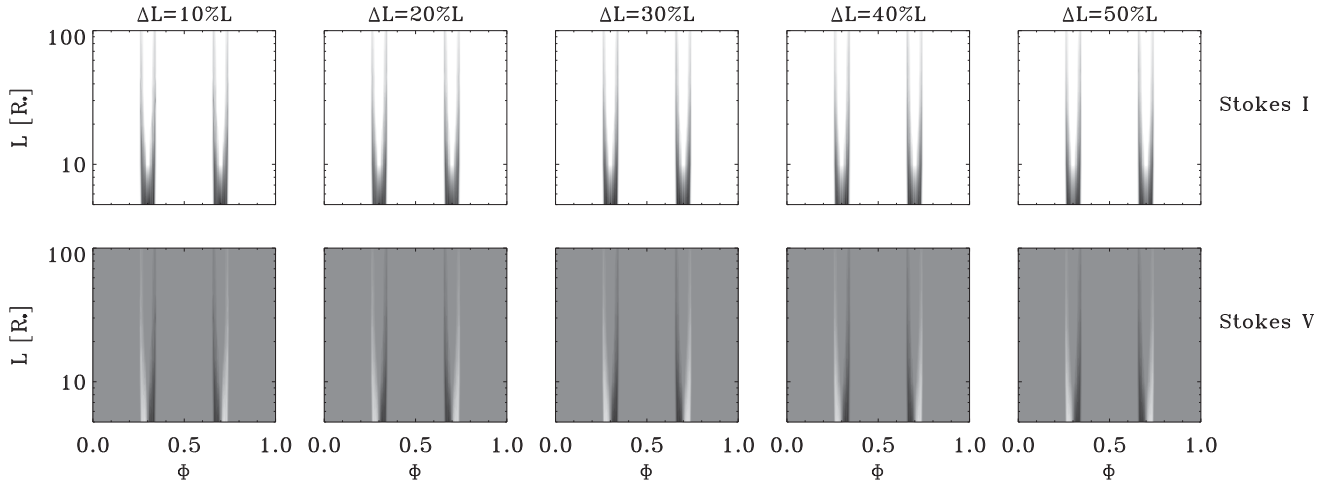
Figure 7. Dynamic auroral light curves as a function of magnetic shell size. Top panels: Stokes *I*; middle panel: Stokes *V*. The simulations have been performed by varying the equatorial extension of the magnetospheric cavity where the auroral radio emission takes place (defined by the *L*-shell parameter) and the corresponding shell thickness.

increases, the two simulated pulses become clearly doubly peaked, each single peak becoming progressively thinner. Each component is clearly related to a specific stellar hemisphere, as recognizable from the sign of the simulated light curves for Stokes *V* in the middle panels of Fig. 7. The thinning of the pulse with increasing magnetic shell size is the consequence of the progressive decrease of the auroral ring radius associated with a specific radio frequency (as an extreme case, for a magnetic shell with infinite *L*-shell parameter, the auroral region degenerates to a point located on the magnetic axis) and consequently the number of grid points that are sources of detectable ECM emission progressively decreases. This set of simulations highlights that ECM features do not depend on the ratio $\Delta L/L$.

3.4 Dependence on the stellar geometry

To highlight the role of the stellar geometry in auroral radio emission detectability, a set of model simulations has been performed by varying the angle β. After setting the auroral shell size ($L = 15R_*$ and $\Delta L = 20$ per cent of *L*), we performed simulations at $\nu = 1.4$ GHz (beam pattern defined by $\delta = 20°$ and $\theta = 10°$), varying the magnetic axis obliquity (β) from 0°–360° (with a simulation step of 1°). The magnetic polar strength and rotation axis inclination were left unchanged ($B_p = 3000$ G, $i = 43°$).

The variation of the β parameter affects the features of the ECM light curves and the stellar magnetic field curve significantly. We then compared the simulated ECM light curves with the corresponding effective magnetic field curve. The dynamic light curves and the magnetic curves are displayed in Fig. 8 as a function of β. The effective magnetic field is displayed in the top panel of the figure and the other two panels show the Stokes *I* and *V* auroral radio emission (bottom and middle panels of Fig. 8, respectively).

By looking at Fig. 8, it is evident that the ECM light curve features depend on the stellar geometry adopted. In particular, the detectability of the auroral radio emission and the phase separation between the two simulated pulses is a function of β. When the magnetic axis is aligned with the rotation axis ($\beta = 0°$ or $\beta = 180°$), the effective magnetic field does not vary. The effective magnetic field strength has a positive constant value for $\beta = 0°$ (northern hemisphere prevailing) and a negative value for $\beta = 180°$ (southern hemisphere prevailing). When the magnetic obliquity increases, the

effective magnetic field changes as the star rotates. For $\beta = 90° - i = 47°$, the magnetic field curve is characterized by one null at $\Phi = 0.5$. When β is close to this value, the light curve of the auroral radio emission is characterized by only one pulse per stellar rotation, right-hand circularly polarized, centred at $\Phi = 0.5$. As the magnetic obliquity increases, the effective magnetic field inverts its sign twice at every stellar rotation. Therefore, we simulated two doubly peaked ECM pulses.

At $\beta = 90°$, the pulse separation increases up to $\Delta\Phi = 0.5$, where it starts to decrease. For $\beta = 180° - i = 133°$, the magnetic field curve again has a single null, but at $\Phi = 0$. When the misalignment between the magnetic and rotation axis is close to this value, the light curve of the auroral radio emission shows a single large pulse, left-hand circularly polarized and centred at $\Phi = 0$. Beyond this limit of β, the auroral radio emission vanishes. The exact limits of the range of β able to give detectable auroral radio emission also depend on the ray-path deflection θ. The simulations performed when β lies in the range 180°–360° closely resemble the behaviour simulated in the range 0°–180°, but with the opposite sign of B_e. Consequently, a swap of circular polarization occurs (middle and top panels of Fig. 8). As a result of the present analysis, it can be seen that the capability of detecting ECM radiation is marginal for those stars that do not change the net polarity of the effective magnetic field on the observer's line of sight.

The beam pattern chosen to perform the present analysis is upward-deflected. The simulated ECM radio light curves are then characterized by contributions from the two opposite hemispheres that are clearly distinguishable by the sign of the simulated Stokes *V* parameter. If the ray path is not deflected ($\theta = 0$), the simulated auroral radio emission is unpolarized (Stokes $V = 0$). The Stokes *I* light curve is instead characterized by two single peaks occurring at phases (Φ_0 and $1 - \Phi_0$) that represent stellar orientations characterized by the magnetic axis being perpendicular to the line of sight ($B_e = 0$), according to the analysis performed in Section 3.1. In this case, the detection of auroral radio emission from a star can be used to fix the oblique rotator geometry (β), the rotation axis inclination *i* being known. In fact, on the basis of simple dipolar geometry, from equation (1) the following relation can be derived:

$$\beta = \arctan\left(-\frac{1}{\tan i \cos \Phi_0}\right). \qquad (2)$$
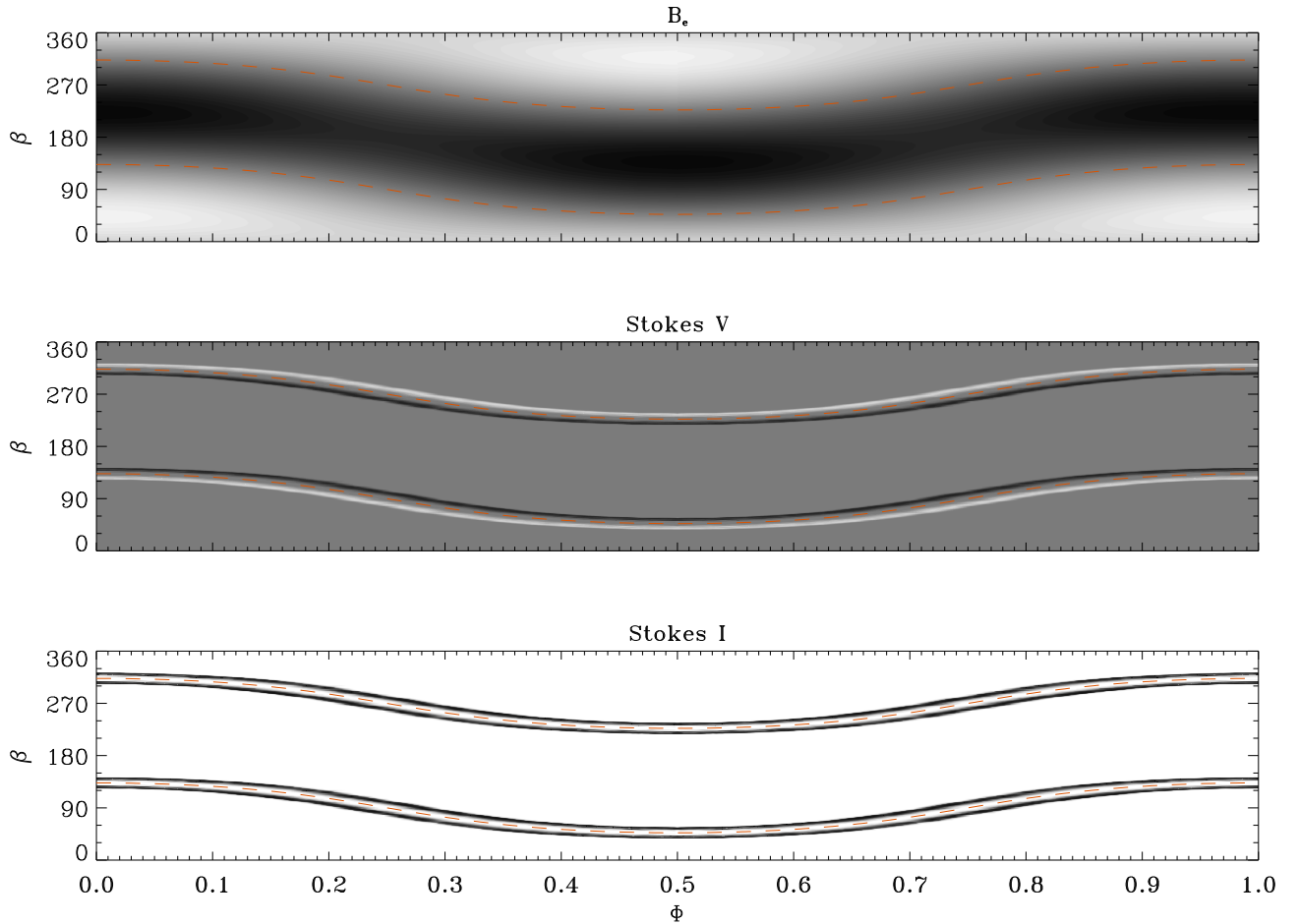
Figure 8. Variations of the effective magnetic field curve and auroral light curve as a function of the misalignment between the magnetic and rotation axis orientations (angle β). Top panel: dynamic effective magnetic field curves. Middle panel: dynamic auroral light curves for Stokes *V*. Bottom panel: dynamic auroral light curves for Stokes *I*. The dashed lines indicate the values of β that locate the nulls of the magnetic effective curve at fixed values of stellar rotational phase, obtained using equation (2).

Given the rotation axis inclination, the equation above returns those values of β for which the effective magnetic field curve is zero at Φ_0. The results of equation (2), obtained assuming $i = 43°$, have been superimposed on the model simulation in Fig. 8. It can be seen that the curves β versus Φ_0 are intermediate between the tracks left by the characteristic double peaks of opposite polarity, which are a signature of deflected ECM emission (middle and bottom panels of Fig. 8). Therefore, in the case of auroral radio emission characterized by ray-path deflection ($\theta > 0$), it is also possible to obtain the ORM geometry. This is because if the ECM contributions arising from the two opposite stellar hemispheres are clearly detected, then the stellar rotational phase related to a null of the effective magnetic field can be located in the middle between the phases of occurrence of coherent peaks with opposite Stokes *V* sign.

4 DISCUSSION AND CONCLUSIONS

The purpose of the model described in this article is the simulation of auroral radio emission from stars characterized by a dipole-like magnetic field. Auroral radio emission is a well-known phenomenon common to the magnetized planets of the Solar system (Zarka 1998) and also present in some kinds of magnetic star (Trigilio et al. 2011; Nichols et al. 2012). The mechanism responsible for this kind of radio emission is the coherent amplification

mechanism known as ECM. The modelling of ECM emission has been developed in accordance with the laminar source model (Louarn & Le Queau 1996a,b). In this case, the auroral radio emission is constrained within a narrow beam directed tangentially along the cavity boundary. This kind of anisotropic beaming is able to reproduce successfully the timing and pulse width of the auroral radio emission observed from the early-type star CU Vir (SP A0V) (Trigilio et al. 2011; Lo et al. 2012). Moreover, at the bottom of the main sequence, the presence of ECM emission characterized by strongly anisotropic beaming has been confirmed in the case of ultracool dwarfs (SP > M7) (Lynch, Mutel & Güdel 2015).

The dependence of auroral radio emission features on model parameters has been analysed extensively. Despite the simplified assumption of a pure dipole characterizing the stellar magnetic field, this model is a powerful tool to study how the timing and pulse profile depend on the parameters that define the source geometry and the parameters that control the beam pattern. The analysis in this article allows us to draw some general conclusions that help us to interpret the features observed in auroral radio emission from individual stars.

First of all, we point out how the recurrence phases of the ECM pulses are related to the features of the magnetic curve. In the case of auroral radio emission propagating perpendicularly to the magnetic field vector, we obtain unpolarized coherent pulses coinciding exactly with the nulls of the effective magnetic field curve, since

RCP and LCP rays have the same direction. This coincidence ceases as the ECM beam pattern deflects. In this case, each single auroral radio pulse becomes doubly peaked, because the two polarizations are deflected differently. As a consequence of the magnetic polarity of the stellar hemisphere where the ECM emission arises, the peak components are circularly polarized with opposite polarization senses.

In particular, two components of opposite polarization sense occur at phases slightly preceding or following the effective magnetic field null. The phase separation between the two polarized components can be a function of model parameters such as the ray-path deflection, beam opening angle or magnetic shell size. In all cases, the two components are symmetric with respect to the magnetic field null phase.

As a further result of our simulation, we found that once we set the size of the magnetic shell where the auroral radio emission takes place, the distance from the surface and hence the size of the auroral ring does not affect the simulated pulse profile and its localization in phase. It has also been established that the magnetic shell thickness has negligible effects on the light-curve features. Moreover, the size of the magnetic shell does not affect the timing of the auroral pulses, while it does have an influence on the pulse profile. In particular, if auroral radio emission is generated very close to the magnetic dipole axis, as in the case of very small auroral rings related to large magnetospheric shells, the ECM arising from each stellar hemisphere has a very narrow pulse width. We can conclude that, once we have defined the magnetic shell and fixed the beaming of the ECM emission, all auroral radio frequencies that originate from regions located at different heights above the stellar surface are characterized by similar light curves. Regarding the model parameters analysed above, we can conclude that auroral radio emission features are frequency-independent in the sense that, once we have fixed the parameters that control the beam pattern, the location above the poles of the auroral rings, which are frequency-dependent, has no effect on the modelled auroral radio emission. However, as discussed below, other frequency-dependent effects can take place in ECM stellar radio emission. Moreover, the ECM beam pattern is reasonably related to the auroral ring geometry: roughly speaking, auroral radio emission detectable in a direction strongly misaligned from the plane tangent to the cavity wall should be generated in a large thickness auroral ring; conversely, strongly beamed ECM emission is related to a very thin auroral cavity.

The discovery that the light curve of auroral radio emission does not depend on the height above the surface of the auroral ring where it originates has a direct implication for the parameters that are able to locate it. These parameters are the polar magnetic field strength and the harmonic of the gyrofrequency amplified by the ECM process. From the analysis performed in this article, it follows that the above parameters cannot be deduced directly from the detection of auroral radio emission from a given star only.

Measurement of possible frequency-dependent effects of pulsed auroral radio emission, such as the frequency drift of pulse arrival time, has to be related to a possible propagation effect suffered by auroral radio emission generated at different frequencies (for example, the ambient thermal medium refracts ECM radiation of different frequencies differently, as proposed by Trigilio et al. 2011) or to the intrinsic nature of the basic process that generates ECM amplified radiation (for example, in the case of loss-cone driven ECM emission, the hollow cone opening angle is a function of frequency). In detail, the half-aperture of the hollow cone is defined as follows: $\cos \theta_B = v/c \sqrt{1 - \nu_B/\nu_{B_{max}}}$ (Hess et al. 2008), where, following the resonance condition for gyromagnetic emission at the sth

harmonic, $\nu_B = \nu/s$ (Melrose & Dulk 1982), with $\nu_{B_{max}}$ the gyrofrequency at the stellar surface. We note how the elementary process that gives rise to amplified radiation could affect the propagation direction of the resulting auroral radio emission detected at different frequencies. On the other hand, along its path the ECM radiation originating in a density-depleted region close to the stellar surface passes through refracting cold thermal regions that deflect the propagation direction. The ray-path refraction is described by Snell's law: $\sin \alpha_r = \sin \alpha_i / n_{refr}$, where $n_{refr} = \sqrt{1 - \nu_p^2/(\nu(\nu - \nu_B))}$ is the refraction index of the cold thermal medium travelled by the amplified rays and α_i and α_r are the angles that the incident and the refracted rays form with the line perpendicular to the refractive layer. The refraction plane orientation depends on the shape of such refractive layers; this can introduce a possible further longitudinal deflection to the ray path, giving rise to a possible phase shift of coherent pulses. Moreover, the plasma frequency depends on the density of the thermal plasma (N_e) as follows: $\nu_p = 9 \times 10^{-6}\sqrt{N_e}$ GHz; a possible longitudinal anisotropy of the ambient thermal medium trapped within the stellar magnetosphere could affect the propagation of the two ECM pulses differently. We highlight that comparison between the magnetic curve and the Stokes I and V light curves of auroral radio emission can be used as a diagnostic tool of the environment where the ECM is pumped.

Finally, the simulations performed here allow us to highlight that the main parameter that localizes auroral radio pulses in the phase-folded light curve is the obliquity of the stellar magnetosphere with respect to the rotation axis. As expected, the timing of auroral radio pulses is strictly related to the geometry of the star. Moreover, the magnetic axis orientation is strictly related to the possibility of detecting such a phenomenon. We can conclude that the study of the timing of ECM pulses from stars that show such an elusive phenomenon could be a very useful tool with which to obtain hints about the geometry of the magnetosphere where it takes place, besides its extraordinary importance in the study of the physical conditions able to generate ECM radiation itself.

ACKNOWLEDGEMENTS

REFERENCES

Antonova A., Doyle J. G., Hallinan G., Bourke S., Golden A., 2008, A&A, 487, 317
Berger E., 2002, ApJ, 572, 503
Burgasser A. J., Putman M. E., 2005, ApJ, 626, 486
Chandra P. et al., 2015, MNRAS, 452, 1245
Drake S. A., Abbot D. C., Bastian T. S., Bieging J. H., Churchwell E., Dulk G., Linsky J. L., 1987, ApJ, 322, 902
Ergun R. E., Carlson C. W., McFadden J. P., Delroy G. T., Strangeway R. J., Pritchett P. L., 2000, ApJ, 538, 456
Hallinan G., Antonova A., Doyle J. G., Bourke S., Lane C., Golden A., 2008, ApJ, 684, 644
Hess S., Cecconi B., Zarka P., 2008, Geophys. Res. Lett., 35, 3107
Kochukhov O., Lüftinger T., Neiner C., Alecian E., the MiMeS collaboration 2014, A&A, 565, 83
Leone F., 1991, A&A, 252, 198
Leone F., Umana G., 1993, A&A, 268, 667
Leone F., Trigilio C., Umana G., 1994, A&A, 283, 908
Leto P., Trigilio C., Buemi C. S., Umana G., Leone F., 2006, A&A, 458, 831

Leto P., Trigilio C., Buemi C. S., Leone F., Umana G., 2012, MNRAS, 423, 1766

Linsky J. L., Drake S. A., Bastian S. A., 1992, ApJ, 393, 341

Lo K. K. et al., 2012, MNRAS, 421, 3316

Louarn P., Le Queau D., 1996a, Planet. Space Sci., 44, 199

Louarn P., Le Queau D., 1996b, Planet. Space Sci., 44, 211

Lynch C., Mutel R. L., Güdel M., 2015, ApJ, 802, 106

Melrose D. B., Dulk G. A., 1982, ApJ, 259, 844

Menietti J. D., Mutel R. L., Christopher I. W., Hutchinson K. A., Sigwarth J. B., 2011, J. Geophys. Res. (Space Phys.), 116, 12219

Mutel R. L., Christopher I. W., Pickett J. S., 2008, Geophys. Res. Lett., 35, 7104

Nichols J. D., Burleigh M. R., Casewell S. L., Cowley S. W. H., Wynn G. A., Clarke J. T., West A. A., 2012, ApJ, 760, 59

Oksala M. E., Wade G. A., Townsend R. H. D., Owocki S. P., Kochukhov O., Neiner C., Alecian E., Grunhut J., the MiMeS Collaboration, 2012, MNRAS, 419, 959

Ravi V., Hobbs G., Wickramasinghe D., Champion D. J., Keith M., 2010, MNRAS, 408, L99

Route M., Wolszczan A., 2012, ApJ, 747, L22

Route M., Wolszczan A., 2013, ApJ, 773, 18

Speirs D. C., Bingham R., Cairns R. A., Vorgul I., Kellett B. J., Phelps A. D. R., Ronald K., 2014, Phys. Rev. Lett., 113, 155002

Stevens I. R., George S. J., 2010, in Martí J., Luque-Escamilla P. L., Combi J. A., eds, ASP Conf. Ser. Vol. 422, High Energy Phenomena in Massive Stars. Astron. Soc. Pac., San Francisco, p. 135

Stift M. J., 1973, A&A, 22, 209

Trigilio C., Leto P., Leone F., Umana G., Buemi C., 2000, A&A, 362, 281

Trigilio C., Leto P., Umana G., Leone F., Buemi C. S., 2004, A&A, 418, 593

Trigilio C., Leto P., Umana G., Buemi C. S., Leone F., 2008, MNRAS, 384, 1437

Trigilio C., Leto P., Umana G., Buemi C. S., Leone F., 2011, ApJ, 739, L10

Vorgul I., Helling Ch., 2016, MNRAS, 458, 1041

Williams P. K. G., Berger E., Irwin J., Berta-Thompson Z. K., Charbonneau D., 2015, ApJ, 799, 192

Wu C. S., Lee L. C., 1979, ApJ, 230, 621

Zarka P., 1998, J. Geophys. Res., 103, 20159

This paper has been typeset from a TEX/LATEX file prepared by the author.